Near-infrared coherent Fourier scatterometry for deep subsurface nanostructure metrology in silicon

Paul, Anubhav; Boonstra, Mathijs; Pereira, Silvania F.

DOI
10.1016/j.optlaseng.2025.109354

Publication date
2025

Document Version
Final published version

Published in
Optics and Lasers in Engineering

Citation (APA)
Paul, A., Boonstra, M., & Pereira, S. F. (2025). Near-infrared coherent Fourier scatterometry for deep subsurface nanostructure metrology in silicon. *Optics and Lasers in Engineering*, *195*, Article 109354. https://doi.org/10.1016/j.optlaseng.2025.109354

Optics and Lasers in Engineering 195 (2025) 109354

Contents lists available at ScienceDirect

Optics and Lasers in Engineering

journal homepage: www.elsevier.com/locate/optlaseng

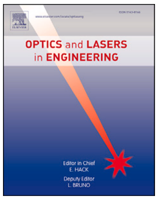

Near-infrared coherent Fourier scatterometry for deep subsurface nanostructure metrology in silicon

Anubhav Paul *, Mathijs Boonstra, Silvania F. Pereira

Imaging Physics Department, Faculty of Applied Sciences, Delft University of Technology, Lorentzweg 1, 2628 CJ, Delft, the Netherlands

ARTICLE INFO

Keywords:
Coherent Fourier scatterometry
Subsurface nanostructure metrology
Optical metrology

ABSTRACT

As advanced packaging evolves with 2.5D/3D integration, the demand grows for the inspection of subsurface nanostructures and defects within silicon (Si), ensuring reliability and yield in modern electronics. In this paper, we demonstrate coherent Fourier scatterometry (CFS) at a near-infrared wavelength ($\lambda = 1055$ nm) for noninvasive inspection of nanostructures buried within Si. Despite Si's transparency in this spectral range, its high refractive index causes strong Fresnel reflections at the air–Si interface. To eliminate these unwanted signals, we employ two distinct approaches: (i) a split detector to subtract reflections in defect inspection mode, and (ii) a reduced coherence length, below lasing threshold, combined with spatial filtering, for retrieving far-field diffraction patterns in grating inspection mode. We systematically investigate how thickness of overlying Si (without overlying Si wafer, with 300 μm thick Si wafer, and with 500 μm thick Si wafer) affects scattering signals of the buried nanostructures. We demonstrate the detection of low contrast polystyrene nanospheres (down to 400 nm, well below the diffraction limit of $\lambda/(2\,\mathrm{NA}) \approx 959$ nm) buried under 500 μm of Si. Further, we successfully detect nanopillars ≥ 100 nm and nanopits ≥ 225 nm. We also analyze the influence of spherical aberrations, which increases linearly with the thickness of the Si layer, resulting in a degradation of the focal spot quality. Beyond isolated defects, we retrieve the diffraction patterns of a 1430 nm period grating under 500 μm of Si, with minimal distortion relative to when no Si layer is present. Overall, these results highlight CFS as a robust, high-sensitivity technique for in-depth inspection in microelectronics and photonic applications, demonstrating potential for failure analysis, process control, and metrology in advanced packaging environments.

1. Introduction

Semiconductor technologies continue to migrate toward complex, high-density three-dimensional (3D) integration, driving a pressing need to inspect and characterize buried nanostructures and defects in silicon (Si) based devices [1,2] such as, 2.5D and 3D packaging leverage stacked dies, microbumps, and through-silicon vias (TSVs) [3]. However, such intricate vertical architectures are increasingly vulnerable to buried defects, such as voids, cracks, inclusions, or partial interconnects, which can form during any of the numerous manufacturing process steps [4–6]. Accurately detecting, localizing, and characterizing these defects at scales below a few hundred nanometers and at depths of tens or even hundreds of micrometers is therefore a pivotal challenge for ensuring reliability and high yield. Beyond electronics, the ability to assess subsurface features is also vital in biomedical, and photonic applications, where sophisticated multilayer designs must be verified for functionality [7,8].

Despite the high demand for buried-structure metrology, current solutions exhibit critical limitations. X-ray microscopy offers nondestructive 3D visualization but often operates with a trade-off between throughput and resolution [9]. Synchrotron-based X-ray sources can achieve submicrometer resolution, yet are largely inaccessible for inline production and can be time intensive [10]. Recent advances in lab-based critical dimension small angle x-ray scattering (CD-SAXS) systems now enable high-precision metrology of periodic nanostructures in a fab-compatible form factor. However, these techniques remain constrained by long acquisition times, limited brightness of compact X-ray sources, and a reliance on model-based inverse reconstruction, restricting their applicability to aperiodic or isolated defects [11]. Scanning acoustic microscopy (SAM) excels at detecting interfaces, delamination, and macro-voids in advanced packages but struggles to achieve submicron resolution for deeply buried, isolated nanoscale features [12,13]. Photoluminescence methods can reveal crystal dislocations or doping-level defects but are typically sensitive to material-specific

---

* Corresponding author.
E-mail address: A.Paul-1@tudelft.nl (A. Paul).

https://doi.org/10.1016/j.optlaseng.2025.109354
Received 2 June 2025; Received in revised form 11 July 2025; Accepted 11 September 2025

luminescence pathways, limiting their general applicability [14]. Furthermore, electron microscopy (EM), although remains the standard due to its high resolution, requires non-invasive sample preparation and milling to expose the sub-surface region of interest [15]. This both prolongs the analysis time and risks of altering delicate defect structures. Atomic force microscopy (AFM) and its variants like ultrasonic force microscopy (UFM), scanning probe microscopy (SPM), and heterodyne force microscopy (HFM) are known for near-surface or thin-film subsurface analyses [16–19]. These techniques can often detect nanoscale features near the top interface by exploiting mechanical, ultrasonic, or thermal contrasts [20–22]. Although it is possible to image extremely small features with these techniques, the effective penetration depth is strongly influenced by the stiffness and damping properties of the sample, making it difficult to consistently resolve deeply buried objects. Furthermore, AFM based approaches are inherently serial, requiring point-by-point scanning over areas of interest, and thus limiting their throughput and suitability for rapid production line monitoring [23].

Infrared (IR) microscopy has emerged as an attractive strategy for subsurface imaging, mainly because Si is transparent at IR wavelengths [13,24]. This transparency opens up the possibility for volumetric inspection under standard wafer-thickness conditions, allowing features buried tens to hundreds of micrometers below the surface to be probed. However, it is constrained by the intrinsic diffraction limit at IR wavelengths, restricting the attainable resolution and making it difficult to precisely characterize sub-micron features. Further, in reflective configurations, strong Fresnel reflections at both the air–Si boundary and the Si–wafer backside often interfere with the relatively weak scattering signals from the buried nanostructures [25]. Such interference can severely degrade signal contrast, hindering parameter retrieval or shape determination for subwavelength features. As a consequence, there remains a critical need for improved techniques that circumvent both the diffraction limit and unwanted interfacial reflections while still providing robust signal-to-noise ratios for deeply buried nanostructures.

Coherent Fourier scatterometry (CFS) offers a promising route to address these challenges. Conventionally used for surface metrology of nanostructures such as gratings, or isolated particles [26,27]. In CFS, the far-field scattered signal is collected and analyzed to retrieve dimensional information without requiring complex modeling of subwavelength nanostructures beyond the diffraction limit [28,29]. In this work, by operating CFS at near-IR wavelength range tailored to Si's transparency and tuning the coherence length of the source, interference from the air–Si boundary can be eliminated. Spatial filters can be combined to further remove these undesired specular reflections, making it feasible to selectively detect scattering from subsurface nanostructures. This balanced approach provides CFS with the ability to locate and characterize subwavelength nanostructures non-destructively, even when they are buried hundreds of micrometers under the wafer surface, in a high-throughput manner. We demonstrate that this method provides strong signal contrast from subsurface defects like low contrast isolated particles, nanopillars, and nanopits, with subwavelength resolution even under 500 μm thick Si wafers. Further, this method can also be used to inspect nanostructures such as gratings buried within 500 μm thick Si layer, which has applications in bonded overlay metrology. Our results highlight the potential of CFS as a versatile metrology solution for 3D-integrated packaging and other applications that require nondestructive, in-depth inspection of buried nanostructures.

2. Methods

2.1. Experimental setup

In this section, we describe the experimental setup of CFS as shown in Fig. 1. A laser diode controller (LDC) drives a near-infrared diode laser ($\lambda = 1055$ nm). The emitted light is coupled into a single-mode fiber (SMF) using a lens (L1), and an off-axis parabolic mirror (OAP M1) collimates the emerging beam. The collimated beam passes through a polarizer (P1), which is used to set the polarization direction of the illumination beam. In the experiments, we use the TE polarization configuration, where the polarization direction of P1 at the pupil is parallel to the y-axis (see Fig. 1). The linearly polarized beam is directed through a nonpolarizing beam splitter (BS1) and then focused onto the sample using a microscope objective (MO) having a numerical aperture (NA) of 0.55, resulting in a focused spot having Airy diameter of $1.22\lambda/\mathrm{NA} = 2.34$ μm. The sample is mounted on a piezocontrolled translation stage (XYZ TS) to scan the sample in the (x, y) plane. The translation stage can be laterally scanned in a serpentine pattern. The scattered light is collected by the same MO and transmitted back through the nonpolarizing beam splitters (BS1 and BS2). A telescopic system composed of two lenses (L2 and L3) relays the light to the back focal plane (BFP) of the MO. A CCD camera positioned at this plane captures the so called far-field signatures, which is the angular spectrum of the scattered waves from all incident plane waves within the focused spot. A pinhole (F1) is placed between L2 and L3, as a spatial filter to selectively remove unwanted scattering from the defocused planes. A split detector (SD) is placed in the BFP of the MO with the help of a mirror (M2) and another telescopic system composed of two lenses (L4 and L5). The split detector consists of two pixels aligned perpendicular to the scan direction, and the intensity from one pixel is subtracted from the other. In defect-free regions of the sample, the scattered far-field pattern (specular reflection) remains reflection symmetric with respect to the illumination polarization direction. This results in nearly equal intensities on both detector halves and a differential signal close to zero. Additionally, the specular reflections from the polished air–Si interface, are also effectively suppressed. As a result, both background specular reflections and system noise are suppressed, and we observe a clean, near-zero baseline. Due to this unique feature we do not need to use a spatial filter in this beam arm. Now, as the focused beam is scanned through a nanostructure placed on the sample, the far field signature becomes asymmetric, and we observe a position-dependent differential signal.

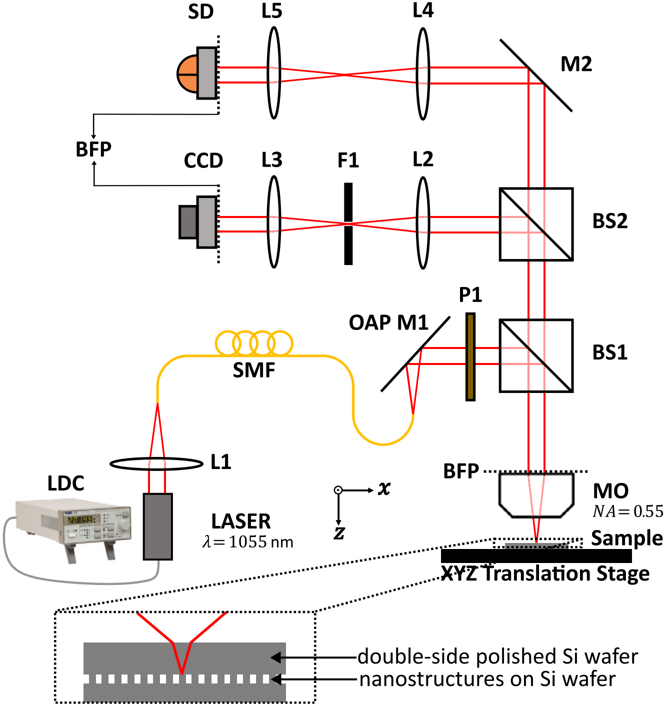

Fig. 1. Schematic of the experimental setup of coherent Fourier scatterometry (CFS).

In the experiments, we investigate samples consisting of nanostructures such as gratings and various types of defects buried within Si. However, fabricating such buried structures with precise control is highly complex [30]. To overcome this challenge, we first measure the nanos-

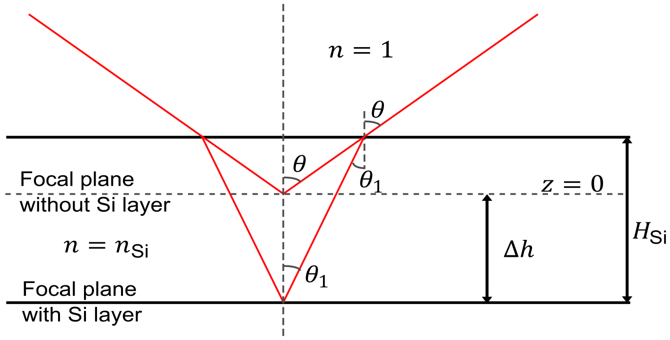

Fig. 2. Schematic illustration of the focal shift when a Si layer of thickness H_{Si} is placed on top of the sample. The red lines represent the maximum cone of light forming the focused spot before (angle θ) and after (angle θ_1) entering the Si layer.

tructures that are fabricated on the Si wafer without any overlying Si layer (sample in its exposed state). Then, to simulate different degrees of buriedness, we place double-side polished Si wafers of varying thicknesses on top of the structures. This approach allows us to systematically study how the overlying Si influences the scattering and far-field signatures, providing insights into the detectability of buried features.

2.2. *Refocusing adjustment for Si layer compensation*

Accurate focusing of the illumination beam onto the nanostructures under investigation is crucial for obtaining reliable experimental results. However, when a Si wafer is placed on top of the sample, the focal plane shifts [31]. As the beam now travels through a medium with a different refractive index, the original focus moves away from the nanostructures, requiring an adjustment in the z-axis to bring the focus back onto the buried nanostructures. To quantify this focal shift, we consider the schematic as illustrated in Fig. 2, which depicts the displacement Δh needed to refocus the beam onto the nanostructures when a Si layer of thickness H_{Si} is introduced. The red lines in the diagram represent the maximum cone of light forming the focused spot. Initially, outside the Si layer, this cone is defined by the angle θ, where, $\sin(\theta) = \mathrm{NA}$. Upon entering the Si layer, the light undergoes refraction due to the difference in refractive indices. The new propagation angle inside the Si is denoted as θ_1, given by, $\theta_1 = \sin^{-1}\left(\frac{\mathrm{NA}}{n_{\mathrm{Si}}}\right)$, where n_{Si} is the refractive index of Si. Since the focal plane inside the Si is determined by the altered beam convergence, the required displacement in the z-axis to refocus the beam onto the buried nanostructures is derived as:

$$\Delta h = H_{\mathrm{Si}}\left(1 - \frac{\tan(\theta_1)}{\tan(\theta)}\right) \tag{1}$$

The equation (1) provides a straightforward method to calculate the necessary focal adjustment based on the Si layer thickness and the numerical aperture (NA) of the objective. By precisely shifting the focus by Δh, we ensure that the beam remains optimally focused on the nanostructures despite the presence of the Si layer, thereby maintaining measurement accuracy and consistency across different sample configurations. For instance, Si wafers of thickness H_{Si} 300 μm and 500 μm, require shifts of Δh approximately 229 μm and 381 μm, respectively.

2.3. *Coherence tuning for interference suppression*

When investigating nanostructures such as gratings, where we retrieve structural parameters using far-field signatures, it is crucial to minimize unwanted interference from reflections at the air-Si interface. Although Si is highly transparent in the near-IR range due to its extremely low absorption coefficient ($\Im(n_{\mathrm{Si}}) = 0.0001114$) at 1055 nm, its high refractive index ($\Re(n_{\mathrm{Si}}) = 3.5575$) causes significant Fresnel reflections at the air-Si boundary. These reflections interfere with the light scattered from the nanostructures, producing interference fringes in the far-field that complicate the data interpretation.

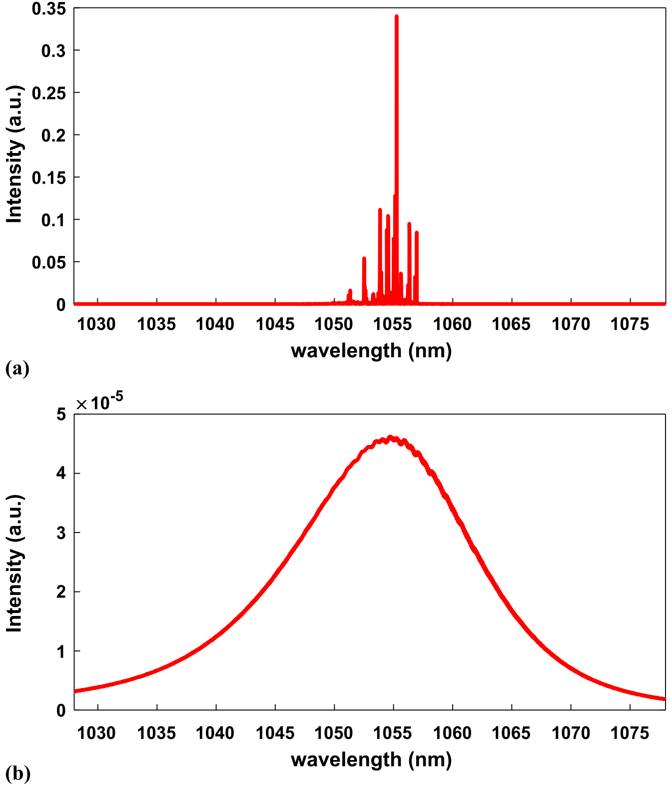

Fig. 3. Laser spectra at two operating conditions. (a) Above the lasing threshold (30 mA), the narrow linewidth results in high coherence length. (b) Below the lasing threshold (17 mA), the broadened spectrum reduces coherence length.

For applications such as grating inspection, where structural parameters are retrieved solving inverse problems from scattering responses, this interference is undesirable. The presence of strong reflections from the air-Si interface introduces additional complexity to the inverse problem, making an already ill-posed problem even harder to solve. To suppress this interference, we tune the coherence length of the laser so that it is shorter than the thickness of the Si layer, ensuring that the reflection from the air-Si interface and the scattering from the nanostructure become mutually incoherent while maintaining sufficient coherence for the coherent scattering of the nanostructures. The coherence length (L_c) is approximated by $L_c = \lambda^2/\Delta\lambda$, where λ is the central wavelength, and $\Delta\lambda$ is the spectral linewidth. We adjust L_c by controlling the driving current of the laser diode controller. Above the lasing threshold (e.g., 30 mA), the laser operates in a narrow spectral mode with a long coherence length ($L_c^{\mathrm{lasing}} = 48392$ μm), maintaining coherence and leading to strong interference. Below the lasing threshold (e.g., 17 mA), the laser spectrum broadens significantly, reducing the coherence length to ($L_c^{\text{non-lasing}} = 61.83$ μm), which is much smaller than the Si layer thickness we use in this study. This effectively removes interference between the reflection and scattered components, ensuring that the far-field signature primarily originates from the nanostructure. This state of the laser, combined with a spatial filter (pinhole), ensures that reflections from the air-Si interface do not distort the far-field signature.

However, for the application of inspection of defects, we operate the laser above the lasing threshold, as the split detector eliminates the specular reflections from the air-Si interface. In Fig. 3, we show the measured laser spectra for both cases: (a) above the lasing threshold (30 mA), showing a narrow linewidth and long coherence length, and (b) below the lasing threshold (17 mA), exhibiting a broadened spectrum and reduced coherence length. These spectra were recorded using an optical spectrum analyzer, Yokogawa AQ6374.

2.4. Sample details

The samples investigated in this work include various nanostructures and defects fabricated on Si substrates. For defect inspection, we use three different samples: (1) a sample with 400 nm polystyrene (PSL) nanospheres deposited on a Si wafer, (2) a sample with 10×2 Si nanopillars, consisting of two rows of cube- and cylinder-shaped nanopillars with lateral nominal dimensions ranging from 100 nm to 1000 nm in 100 nm steps and a nominal height of 250 nm, and (3) a sample with 4×5 etched nanopits on a Si wafer, where the pits have a cubic shape with lateral sizes from 125 nm to 425 nm in 100 nm steps and a nominal height of 160 nm, organized into five rows of identical structures. Further details on the fabrication of these nanostructures can be found in Ref. [29]. For grating inspections, we use a Si grating with a pitch of 1430 nm, with rectangular profile, 50% duty cycle, and height of 160 nm. Additional fabrication details can be found in Ref. [32]. To simulate the buriedness of these nanostructures, we place double-sided polished Si wafers of 300 μm and 500 μm thickness on top of the samples.

3. Results

3.1. Inspection of defects

In this section, we demonstrate the capabilities of CFS for inspecting isolated defects buried within a Si wafer. Here, we detect 400 nm polystyrene (PSL) nanospheres (smaller than the diffraction limit, $\lambda/2NA$) deposited on a Si wafer. To perform defect inspection, we operate the laser above its lasing threshold ($L_c^{\text{lasing}} = 48392$ μm) with a lasing power of 0.5 mW. Our goal is to systematically examine how overlying Si layers affect the scattering signals. We first measure each sample in its exposed state (with no Si wafer on top). To simulate different degrees of buriedness, Si wafers with thicknesses 300 μm and 500 μm are then placed over the sample. After each wafer is added, the focal plane is readjusted by moving the translation stage along the z-axis, as described in Section 2.2. Fig. 4(a) shows an SEM image of a 400 nm PSL nanosphere on Si without any Si wafer on top (SEM imaging cannot be performed through the Si wafer due to limited electron penetration depth). Fig. 4(b)–(d) shows the CFS scans of a 100×100 μm region of 400 nm PSL nanospheres on Si: (b) without Si wafer on top; (c) with 300 μm Si wafer on top; and (d) with 500 μm Si wafer on top. The PSL nanospheres are clearly detected in all cases, illustrating that CFS can effectively inspect defects even under 500 μm of Si. To quantify performance, we calculate the signal-to-noise ratio (SNR) according to

$$\mathrm{SNR_{dB}} = 10\log_{10}\left(\frac{P_{\text{signal}}}{P_{\text{noise}}}\right), \tag{2}$$

where P_{signal} is the power of the signal (contained in the defects) and P_{noise} is the background noise. Table 1 lists the calculated SNR values. Although the SNR is high for all the cases, it decreases slightly as the wafer thickness increases. This is primarily due to aberrations introduced by the additional Si layers, which degrade the focal spot and reduce the Strehl ratio. A more detailed analysis of these aberrations is provided in Appendix A. Further, in the context of our CFS based detection scheme, the detection capability is not governed by the conventional diffraction limit ($\lambda/2\mathrm{NA} \approx 959$ nm) of the system, but rather by the SNR of the scattered signal associated with the defect. That is, defect detection is feasible as long as the defect-induced signal exceeds the system noise floor, even if the defect is subwavelength in size. A comprehensive analysis of CFS regarding minimum detectable signal, noise tolerance, and dynamic range has already been demonstrated by Dmytro et al. [33].

Now, to investigate the limitation of the technique in determining how small the defects can be and still be detected, we consider two types of defects: nanopillars and nanopits. Our samples consist of these nanostructures with varying lateral dimensions, with the smallest defects of dimension $\sim \lambda/10$, as already discussed in section 2.4. The experimental approach is the same as that used for the 400 nm PSL nanospheres, detailed earlier. Fig. 5(a) shows a SEM image of a 100×30 μm region of Si nanopillars without any Si wafer on top, where the top row has nanopillars in the shape of a cylinder, while the bottom row has nanopillars in the shape of a square; the nanopillars have dimensions ranging from 100 nm to 1000 nm (from left to right). The middle row has markers in the shape of '+'. Fig. 5(b)-(d) shows the corresponding 100×30 μm CFS scans of nanopillars: (b) without Si wafer on top; (c) with 300 μm Si wafer on top; and (d) with 500 μm Si wafer on top. We can observe that even the 100 nm ($\sim \lambda/10$) nanopillars are detected in all the different cases, showcasing the capability of CFS to detect ≥100 nm nanopillars buried under 500 μm of Si. In Table 2, we summarize the calculated SNR based on equation (2), for all the different dimensions of nanopillars and different cases. Although the SNR is high in all cases, we observe a decrease in the SNR as the dimension of the Si nanopillars becomes smaller. This is understandable as the signal/scattering strength scales with the dimension of the scatterer. [33]. Additionally, the SNR reduces as the Si wafer on top becomes thicker.

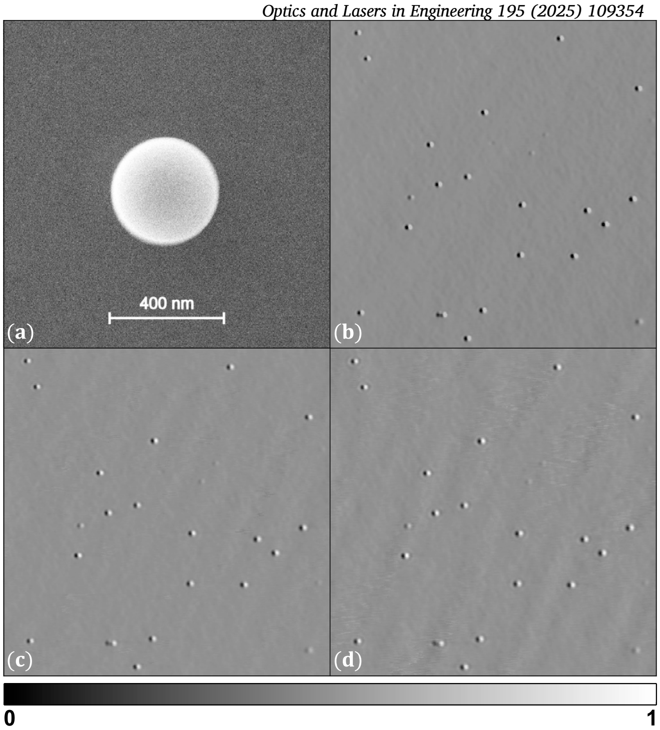

Fig. 4. (a) SEM image of a 400 nm PSL nanosphere on Si with no overlying wafer. (b) CFS scan of a 100×100 μm region showing 400 nm PSL nanospheres on Si with no overlying wafer. (c) CFS scan of the same region with a 300 μm thick Si wafer on top. (d) CFS scan of the same region with a 500 μm thick Si wafer on top.

Table 1
Measured SNR of 400 nm PSL sample.

Case	$\mathrm{SNR_{dB}}$
Without Si wafer on top	26.09
With 300 μm Si wafer on top	25.28
With 500 μm Si wafer on top	23.04

Fig. 6(a) shows a SEM image of a 50×50 μm region of etched nanopits without any Si wafer on top, where all rows have identical nanopits in the shape of a square, with dimensions ranging from 125 nm to 425 nm (from left to right). Fig. 6(b)-(d) shows the corresponding 50×50 μm CFS scans of nanopits: (a) without Si wafer on top; (c) 300 μm Si wafer on top; and (d) with 500 μm Si wafer on top. We can observe that even the 125 nm ($\sim \lambda/10$) nanopillars are detected, in Fig. 6(b),

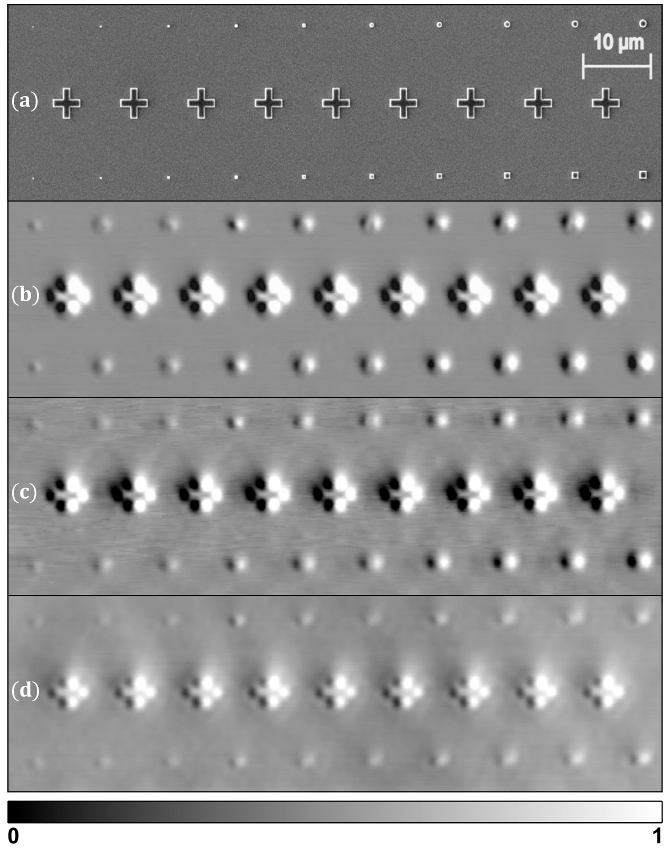

Fig. 5. (a) SEM image of a 100 × 30 µm region showing the Si nanopillars with no overlying wafer. (b) CFS scan of the same region with no overlying wafer. (c) CFS scan of the same region with a 300 µm thick Si wafer on top. (d) CFS scan of the same region with a 500 µm thick Si wafer on top.

Table 2
Measured SNR of Si nanopillars sample.

Dim. (nm)	$\mathrm{SNR_{dB}}$ Without Si wafer on top	With 300 µm Si wafer on top	With 500 µm Si wafer on top
100	12.23	5.91	5.85
200	15.23	12.26	6.64
300	15.32	11.82	6.51
400	19.90	16.20	13.69
500	20.03	15.73	11.77
600	19.76	15.79	10.25
700	21.27	17.69	9.51
800	21.97	18.26	10.97
900	21.69	17.72	12.83
1000	22.15	18.84	13.48

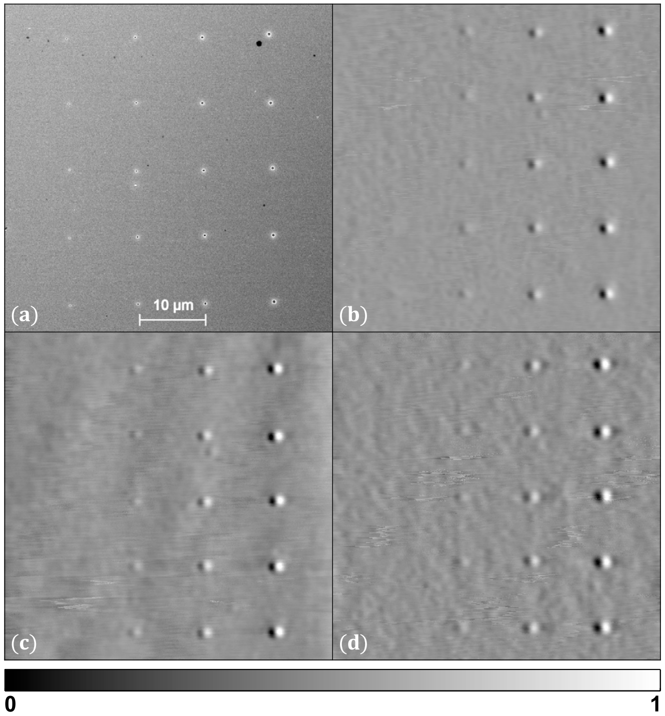

Fig. 6. (a) SEM image of a 50 × 50 µm region showing the etched nanopits with no overlying wafer. (b) CFS scan of the same region with no overlying wafer. (c) CFS scan of the same region with a 300 µm thick Si wafer on top. (d) CFS scan of the same region with a 500 µm thick Si wafer on top.

Table 3
Measured SNR of etched nanopits sample.

Dim. (nm)	$\mathrm{SNR_{dB}}$ Without Si wafer on top	With 300 µm Si wafer on top	With 500 µm Si wafer on top
125	4.07	-	-
225	12.20	10.13	4.92
325	16.64	14.37	13.84
425	19.94	16.95	16.87

where the top Si wafer is not present. However, for all the other cases with the Si wafer on top, we cannot detect 125 nm etched nanopits. This can be due to the aberrations introduced by the intervening Si, which degrade the focus spot and reduce the scattered signal from the nanopits. In contrast, 100 nm nanopillars are detectable under similar conditions, likely due to their greater vertical extent and scattering volume, which enhances their interaction with the focal field and results in a stronger scattered signal. Nevertheless, nanopits with dimensions ≥225 nm remain detectable even through 500 µm of Si. It is important to note that the split detector provides differential contrast based on far-field asymmetry, enabling detection of subwavelength features. However, it does not distinguish between different defect types, such as nanopits and nanopillars, since both produce similar asymmetry signatures. Our approach is focused on universal detection of buried nanoscale features, rather than classification. In Table 3, we summarize the calculated SNR based on equation (2), for all the different dimensions of nanopits and different cases. Similar to the nanopillars, we observe that the SNR decreases as the dimension of the Si nanopits becomes smaller, and as the Si layer becomes thicker.

3.2. *Inspection of gratings*

In this section, we demonstrate the inspection of diffraction gratings buried within Si wafer using CFS. For that, we inspect a diffraction grating defined by geometrical parameters: period (p) = 1430 nm, line width (w) = p/2, height (h) = 160 nm, and bias (b). b is a parameter that is introduced to define the relative position of the grating to the optical axis of the focused beam. Although the definition of the position $b = 0$ can be arbitrary, we define it as the center of the grating line. When the grating interacts with a focused beam, the incident beam is diffracted into multiple diffraction orders, as described by the grating equation [34]. Each diffracted order is mapped to the Fourier plane (the mapping is limited by the NA), where a CCD captures them. A more detailed discussion on the diffraction theory for CFS is provided in supplementary material, section 1 of supplement 1. For the inspection of gratings, as discussed in section 2.3, we operate the laser below the lasing threshold ($L_c^{\text{non-lasing}} = 61.83$ µm), with 2.5 µW of lasing power. This broadens the laser linewidth and reduces the temporal coherence of the

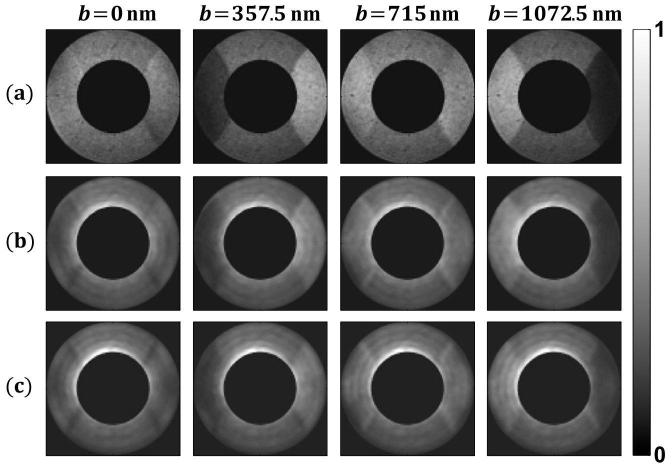

Fig. 7. Far-field signatures of grating with period (p) of 1430 nm, at four bias positions ($b = 0$ nm, 357.5 nm, 715 nm, 1072.5 nm); (a) with no overlying wafer, (b) with a 300 μm thick Si wafer on top, and (c) with a 500 μm thick Si wafer on top.

illumination, which is critical for suppressing interference between the air–Si interface reflection and the grating diffraction orders. The far-field images with this interference demonstrating the effect of coherence is provided in supplementary material, section 2 of supplement 1. We also use a spatial filter in the form of a pinhole to remove the reflected signal from the air-Si interface. This blocks most of the unwanted signal coming from the defocused planes, however, some residual light passes through the center of the pinhole, appearing in the central part of the far-field. For this, we crop the central region of the far-field signatures. Similar to our previous measurements with 400 nm PSL nanospheres, we begin by measuring the grating in its exposed state (without any Si wafer on top). We then place Si wafers of 300 μm and 500 μm thickness on top to simulate different degrees of buriedness, adjusting the focal plane via the z-axis translation stage as detailed in section 2.2. The sample is mounted on an XYZ piezo stage such that the grating lines are parallel to the y-axis at the pupil, and the far-field is captured for various bias positions ($b = 0$ nm, 357.5 nm, 715 nm, 1072.5 nm) within one period of the grating. Fig. 7(a) shows the far-field signatures for different bias positions without any Si wafer on top. As bias (b) is introduced, the interference between the overlapping orders changes [26], resulting in different intensities in the overlapping region. Figs. 7(b) and 7(c) show the corresponding far-field signatures for different bias positions with 300 μm and 500 μm thick Si wafer on top, respectively. We observe that for all the different cases, we obtain the same complete far-field information without any unwanted interference from reflections at the air-Si interface, showcasing the capability of CFS to inspect gratings buried below through 500 μm of Si.

4. Conclusions

In this work, we employed coherent Fourier scatterometry (CFS) in the near-infrared (near-IR) wavelength range ($\lambda = 1055$ nm) to inspect nanostructures buried within Si wafers. Although Si becomes highly transparent in this spectral range due to its negligible absorption coefficient, its large refractive index still introduces strong Fresnel reflections at the air–Si interface. To mitigate this unwanted specular reflection, we employed two distinct approaches tailored to specific measurement objectives: (i) for defect inspection, where we want to detect and localize them, we utilized a split detector to subtract intensities between two detector regions, effectively eliminating reflections from the air–Si boundary. (ii) For grating inspection, where we want to retrieve geometrical parameters from far-field signatures, we reduced the laser's coherence length (operating below the lasing threshold) so that reflections from the air–Si interface do not interfere with the scattering from buried structures, then further filtered out residual reflections using a spatial filter. Using these methods, we systematically investigated how overlying Si affects scattering signals by initially measuring each sample in an "exposed" configuration (without overlying Si layer), then added burial depths by placing 300 μm and 500 μm Si wafers on top of the nanostructures and refocusing accordingly. Our experiments demonstrate that CFS can detect low-contrast polystyrene (PSL) nanospheres, as small as 400 nm (below the diffraction limit of $\lambda/(2\,\mathrm{NA}) \approx 959$ nm), through at least 500 μm of Si with SNR > 20 dB. We further investigated the limitations in the detection capabilities concerning the size of the defects, by measuring two types of defects of varying dimensions: nanopillars with lateral dimensions ranging from 100 to 1000 nm; and nanopits with lateral dimensions ranging from 125 to 425 nm. In both cases, we observed that smaller features exhibit weaker scattering and are more susceptible to wavefront aberrations introduced by the Si. While ≥100 nm nanopillars are still detectable through 500 μm of Si, 125 nm nanopits are not. Nonetheless, pits of ≥225 nm remain visible at the same burial depth. Zemax simulations revealed that only spherical aberration (Zernike term Z9) is introduced by the Si wafer, increasing linearly with thickness. This aberration impacts the focal spot quality, reducing the SNR as the wafer thickness increases. Beyond isolated defects, we demonstrated that with CFS, one can obtain the far-field diffraction patterns of a 1430 nm period grating buried under up to 500 μm of Si, with minimal distortion relative to the uncovered state. While structural parameter retrieval from the measured angular spectrum is not performed in this work, it follows standard model-based fitting procedures demonstrated in prior CFS studies [26]. The focus of this paper is to demonstrate the feasibility of collecting high-fidelity scattering data from buried structures, enabling such reconstruction in future work which involve quantitative extraction of grating parameters (e.g. height, pitch, and line width) from buried nanostructures. By integrating aberration compensation elements, combined with higher NA focusing optics, the focus spot can be optimized at any depth [35], and smaller features can be inspected even at deeper depths. Overall, these findings broaden the scope of CFS to include non-destructive inspection of deeply buried nanostructures in Si. Potential applications include failure analysis in microelectronics, quality control in advanced packaging, and metrology of photonic integrated circuits, where accurate dimensional characterization of embedded features is essential. By enabling high-resolution imaging and diffraction-based measurement through thick Si substrates, CFS opens new avenues for both research and industrial metrology in semiconductor manufacturing and photonic device engineering.

CRediT authorship contribution statement

Anubhav Paul: Writing – review & editing, Writing – original draft, Visualization, Software, Methodology, Investigation, Formal analysis, Data curation, Conceptualization. **Mathijs Boonstra:** Methodology, Investigation. **Silvania F. Pereira:** Writing – review & editing, Supervision, Project administration, Funding acquisition, Conceptualization.

Funding

Nederlandse Organisatie voor Wetenschappelijk Onderzoek (Project 17-24 Synoptics No. 2).

Declaration of competing interest

The authors declare the following financial interests/personal relationships which may be considered as potential competing interests: Anubhav Paul reports financial support was provided by Nederlandse Organisatie voor Wetenschappelijk Onderzoek (Project 17-24 Synoptics No. 2). If there are other authors, they declare that they have no known competing financial interests or personal relationships that could have appeared to influence the work reported in this paper.

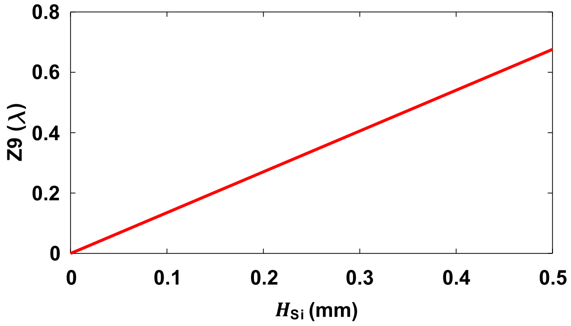

Fig. A.8. Variation in spherical aberration (Z9) as a function of the Si wafer thickness H_{Si} based on Zemax simulations.

Acknowledgement

We would like to thank Roland Horsten and Thim Zuidwijk of TU Delft for the technical support. We also thank Sarika Soman of TU Delft and Thomas Siefke of FSU Jena for fabricating the samples and Thomas Scholte of TU Delft for the SEM images. We would also like to thank Rishav Kumar of TU Delft for his support in Zemax simulations.

Appendix A. Aberrations

In this section, we present a detailed analysis of the wavefront aberrations induced when a focused laser beam passes through a Si wafer using Zemax optical design software [36]. To mimic the experimental conditions, we model a linearly polarized plane wave of wavelength 1055 nm, illuminating the objective lens having NA of 0.55. The objective focuses the light on the focal plane, where we add a Si wafer having thickness H_{Si}. We move the Si such that the beam focuses on the back surface of the wafer. We then evaluated the wavefront aberrations in this focal plane for varying thicknesses of the Si wafer. More details about the design parameters have been provided in the supplementary material, section 3 of supplement 1. We observe that only spherical aberration (Zernike term Z9) is introduced in the wavefront because of the wafer [37]. Fig. A.8 shows the relative variation in Z9 as we increase the thickness H_{Si} of the wafer, where we see that Z9 increases linearly with thickness. This trend indicates that in inspecting nanostructures through even thicker Si layers, compensating for the resulting spherical aberrations will be crucial for achieving a high quality of the focused spot.

Appendix B. Supplementary material

Supplementary material related to this article can be found online at https://doi.org/10.1016/j.optlaseng.2025.109354.

Data availability

Data underlying the results presented in this paper are not publicly available at this time but may be obtained from the authors upon reasonable request.

References

[1] Mansfield E, Barnes B, Kline RJ, Vladar AE, Obeng YS, Davydov A. International roadmap for devices and systems$^{\mathrm{TM}}$ 2023 edition metrology. https://irds.ieee.org/editions/2023, 2023.

[2] Bogdanowicz J, Charley A-L, Leray P, Liu R. 3D metrology and inspection to enable the rise of stacked transistors, wafers, and chips. Metrology, inspection, and process control XXXIX, vol. 13426. SPIE; 2025. p. 8–15.

[3] Li Y, Goyal D. 3D microelectronic packaging: from architectures to applications, vol. 64. Springer Nature; 2020.

[4] Shekhawat GS, Dravid VP. Nanoscale imaging of buried structures via scanning near-field ultrasound holography. Science 2005;310(5745):89–92.

[5] Kassamakov I, Grigoras K, Heikkinen V, Hanhijärvi K, Aaltonen J, Franssila S, et al. Nondestructive inspection of buried channels and cavities in silicon. J Microelectromech Syst 2012;22(2):438–42.

[6] van Es MH, Mohtashami A, Piras D, Sadeghian H. Image-based overlay and alignment metrology through optically opaque media with sub-surface probe microscopy. Metrology, inspection, and process control for microlithography XXXII, vol. 10585. SPIE; 2018. p. 155–62.

[7] Yin J-f, Bai Q, Zhang B. Methods for detection of subsurface damage: a review. Chin J Mech Eng 2018;31:1–14.

[8] Zhu J, Liu J, Xu T, Yuan S, Zhang Z, Jiang H, et al. Optical wafer defect inspection at the 10 nm technology node and beyond. Int J Extrem Manuf 2022;4(3):032001.

[9] Schmidt C. 3-D X-Ray imaging with nanometer resolution for advanced semiconductor packaging FA. IEEE Trans Compon Packag Manuf Technol 2018;8(5):745–9.

[10] Yablon D. Metrology capabilities keep up with semiconductor industry push into 3D integrated circuits (Part 1). https://analyticalscience.wiley.com/content/article-do/metrology-capabilities-keep-%E2%80%A8up-semiconductor-industry-push-into-3d-integrated-circuits, 2024.

[11] Wu W, Kline R Joseph, Jones RL, Lee H-J, Lin EK, Sunday DF, et al. Review of the key milestones in the development of critical dimension small angle x-ray scattering at National Institute of Standards and Technology. J Micro/Nanopatt Mater Metrol 2023;22(3):031206.

[12] Quesson B, Van Willigen D, Hörchens L, Gerritsma A, Bogdanowicz J, Chen C, et al. Feasibility of detecting and imaging deeply buried voids using GHz half wavelength contact acoustic microscopy. In: 2024 IEEE ultrasonics, ferroelectrics, and frequency control joint symposium (UFFC-JS). IEEE; 2024. p. 1–3.

[13] Kong LW, Krueger P, Zschech E, Rudack AC, Arkalgud S, Diebold AC. Sub-imaging techniques for 3D-interconnects on bonded wafer pairs. AIP conference proceedings, vol. 1300. American Institute of Physics; 2010. p. 221–8.

[14] Duru R, Le-Cunff D, Cannac M, Laurent N, Dudas L, Kiss Z, et al. Photoluminescence for in-line buried defects detection in silicon devices. In: 2017 28th annual SEMI advanced semiconductor manufacturing conference (ASMC). IEEE; 2017. p. 262–6.

[15] Frase CG, Buhr E, Dirscherl K. CD characterization of nanostructures in SEM metrology. Meas Sci Technol 2007;18(2):510.

[16] Kimura K, Kobayashi K, Matsushige K, Yamada H. Imaging of Au nanoparticles deeply buried in polymer matrix by various atomic force microscopy techniques. Ultramicroscopy 2013;133:41–9.

[17] Shekhawat G, Srivastava A, Avasthy S, Dravid V. Ultrasound holography for noninvasive imaging of buried defects and interfaces for advanced interconnect architectures. Appl Phys Lett 2009;95(26).

[18] van Es MH, Mohtashami A, Thijssen RM, Piras D, van Neer PL, Sadeghian H. Mapping buried nanostructures using subsurface ultrasonic resonance force microscopy. Ultramicroscopy 2018;184:209–16.

[19] Cuberes MT, Assender H, Briggs G, Kolosov O. Heterodyne force microscopy of PMMA/rubber nanocomposites: nanomapping of viscoelastic response at ultrasonic frequencies. J Phys D, Appl Phys 2000;33(19):2347.

[20] Perrino AP, Ryu Y, Amo CA, Morales M, Garcia R. Subsurface imaging of silicon nanowire circuits and iron oxide nanoparticles with sub-10 nm spatial resolution. Nanotechnology 2016;27(27):275703.

[21] Crozier K, Yaralioglu G, Degertekin F, Adams J, Minne S, Quate C. Thin film characterization by atomic force microscopy at ultrasonic frequencies. Appl Phys Lett 2000;76(14):1950–2.

[22] Yao A, Kobayashi K, Nosaka S, Kimura K, Yamada H. Visualization of Au nanoparticles buried in a polymer matrix by scanning thermal noise microscopy. Sci Rep 2017;7(1):42718.

[23] Chein W-H, Pandey G, Das S, Chen L-C. Advancements in metrology for advanced semiconductor packaging. Optics and photonics for advanced dimensional metrology III, vol. 12997. SPIE; 2024. p. 127–43.

[24] Rudack AC, Kong LW, Baker GG. Infrared microscopy for overlay and defect metrology on 3d-interconnect bonded wafers. In: 2010 IEEE/SEMI advanced semiconductor manufacturing conference (ASMC). IEEE; 2010. p. 347–52.

[25] Trigg A. Applications of infrared microscopy to IC and MEMS packaging. IEEE Trans Electron Packag Manuf 2004;26(3):232–8.

[26] Kumar N, Petrik P, Ramanandan GK, El Gawhary O, Roy S, Pereira SF, et al. Reconstruction of sub-wavelength features and nano-positioning of gratings using coherent Fourier scatterometry. Opt Express 2014;22(20):24678–88.

[27] Roy S, Assafrao AC, Pereira SF, Urbach HP. Coherent Fourier scatterometry for detection of nanometer-sized particles on a planar substrate surface. Opt Express 2014;22(11):13250–62. https://doi.org/10.1364/OE.22.013250. https://opg.optica.org/oe/abstract.cfm?URI=oe-22-11-13250.

[28] Paul A, Rafighdoost J, Dou X, Pereira SF. Investigation of coherent Fourier scatterometry as a calibration tool for determination of steep side wall angle and height of a nanostructure. Meas Sci Technol 2024;35(7):075202.

[29] Paul A, Wever R, Soman S, Pereira SF. Utilizing focused field as a probe for shape determination of subwavelength structures via coherent Fourier scatterometry. Phys Rev Appl 2025;23(2):024016.

[30] Gambino JP, Adderly SA, Knickerbocker JU. An overview of through-silicon-via technology and manufacturing challenges. Microelectron Eng 2015;135:73–106.

[31] Ling H, Lee S-W. Focusing of electromagnetic waves through a dielectric interface. J Opt Soc Am A 1984;1(9):965–73.

[32] Siefke T, Siaudinyté L, Jensen S, Rømer A, Hansen P. Fine details of structural deviations in reference samples for scatterometry. In: Proc. of 19th IMEKO TC10

conference MACRO meets NANO in measurement for diagnostics, optimization and control; 2023.

[33] Kolenov D, Zadeh IE, Horsten RC, Pereira SF. Direct detection of polystyrene equivalent nanoparticles with a diameter of 21 nm (∼ $\lambda/19$) using coherent Fourier scatterometry. Opt Express 2021;29(11):16487–505. https://doi.org/10.1364/OE.421145. https://opg.optica.org/oe/abstract.cfm?URI=oe-29-11-16487.

[34] Paul A, Kolenov D, Scholte T, Pereira SF. Coherent Fourier scatterometry: a holistic tool for inspection of isolated particles or defects on gratings. Appl Opt 2023;62(29):7589–95.

[35] Török P, Varga P, Laczik Z, Booker G. Electromagnetic diffraction of light focused through a planar interface between materials of mismatched refractive indices: an integral representation. J Opt Soc Am A 1995;12(2):325–32.

[36] Ansys *Zemax OpticStudio*, Available from https://www.ansys.com/products/optics/ansys-zemax-opticstudio.

[37] Braat J. Analytical expressions for the wave-front aberration coefficients of a tilted plane-parallel plate. Appl Opt 1997;36(32):8459–67. https://doi.org/10.1364/AO.36.008459. https://opg.optica.org/ao/abstract.cfm?URI=ao-36-32-8459.